Planetary and Space Science 186 (2020) 104917

Contents lists available at ScienceDirect

Planetary and Space Science

journal homepage: www.elsevier.com/locate/pss

Formation of long-distance water ice avalanches on Mars

S.S. Krasilnikov [a,b,*], R.O. Kuzmin [a,c], Y. Bühler [d], E.V. Zabalueva [a]

[a] Vernadsky Institute of Geochemistry and Analytical Chemistry RAS, Moscow, 119334, Russia
[b] Max Planck Institute for Solar System Research, Göttingen, 37077, Germany
[c] Space Research Institute RAS, Moscow, 117997, Russia
[d] WSL Institute for Snow and Avalanche Research, SLF, Davos Dorf, 7260, Switzerland

ARTICLE INFO

Keywords:
Mars
Water ice
Down-slope movement
Avalanche
Moraine
Catastrophic down-slope movement

ABSTRACT

At the high northern latitudes of Mars, there are two impact craters (70.3°N 266.45°E and 67.25°N 249.45°E) with lobate moraine-like ridges (LMLR) on the inner slopes. In addition to these craters, a nearby plain (74°N 95°E) also displays remnants of water ice layered deposits with similar series of lobate ridges. The formation of these ridges has been hypothesized to be caused by either viscoplastic flow of CO_2 ice deposits or a catastrophic down-slope movement of an H_2O ice massif, which produced long-distance avalanches or fast-running glacier surges. In past climatic epochs, the formation of water ice massifs on high latitudes was possible under low (<20°) planet obliquity. Destabilization of water ice massifs on the craters' steep inner slopes could lead to down-slope movement, followed by the destruction of the massifs and the production of long-distance water ice avalanches or surges. In this work, we focus on the avalanche formation hypothesis. The down-slope movement of a water ice massif has several possible causes, with the main one being excessive accumulation of water ice on slopes, which then reaches a critical unstable condition. Modeling of long-distance avalanche processes in Martian environments was carried out with Rapid Mass Movement Simulation (RAMMS:AVALANCHE) software, using the graph-analytical method of estimating avalanche velocity and maximum distance. As a result of the modeling, the volume of down-slope movement was defined, confirming the that LMLR were formed by the catastrophic down-slope movement of H_2O ice masses in the form of long-distance avalanches.

1. Introduction

The subject of our conducted investigation is the morphological character of lobate ridges, resembling glacial moraines, located on the southeastern parts of two impact craters (70.3°N 266.45°E, crater A, and 67.25°N 249.45°E, crater B) (Figs. 1–2), as well as similar landforms on the northern plain 74°N 95°E, site C (Fig. 3). The objects in crater A were initially described by Garvin et al. (2006), while the morphology and origin of the ridges in both craters is discussed in Kreslavsky and Head (2011). The origin of ridges in site C (described below) was first mentioned in Kreslavsky and Head (2007).

These landforms consist of series of lobate moraine-like ridges (LMLR, Fig. 2) located on the southeastern inner slopes of the craters. On the outer southeastern slopes of both craters' rims, several concentric moraine-like ridges (CMLR) (Fig. 2) can be found. These moraine-like ridges in the craters are 15–80 m in width (Kreslavsky and Head, 2011), and do not exceed 30 m in height (Garvin et al., 2006). At all sites, the ridges have a maximum length of approximately 5–7 km and a width of about 1.5–10 km (Kreslavsky and Head, 2011). Fig. 2 demonstrates the area of the modeled ice sheet. This area is clearly visible in the CTX images (Malin et al., 2007) and can be described as a steep and smooth surface, with moraine ridges starting from the lower margin.

At 74°N 95°E on the north plain (site C), there are H_2O ice remnants with a layered structure, typical of northern polar layered deposits (NPLD) (Krasilnikov et al., 2018). This ice massif is ~400 m in height and ~5 km long in the downslope direction, with an average slope of less than ~6°. To the northwest of the ice massif edge (~10–20 km), there is a series of LMLRs (Fig. 3). Their orientation (to the northwest), morphology and number of ridges indicate the same formation process as the LMLRs in the studied craters.

The LMLR features are represented in six ridge sequences in crater A, three main ridge sequences in crater B, and five series of ridge sequences around the remnants of water ice deposits on the northern plain, site C.

Both craters (A and B) are located in the interior unit of the geologic province of Vastitas Borealis (ABvi, (early-Amazonian age)) and the Vastitas Borealis marginal unit (ABv_m, (early-Amazonian age)) (Scott

* Corresponding author. Vernadsky Institute of Geochemistry and Analytical Chemistry RAS, Moscow, 119334, Russia.
E-mail address: krasilnikovruss@gmail.com (S.S. Krasilnikov).

https://doi.org/10.1016/j.pss.2020.104917
Received 26 December 2018; Received in revised form 12 March 2020; Accepted 23 March 2020
Available online 25 March 2020
0032-0633/

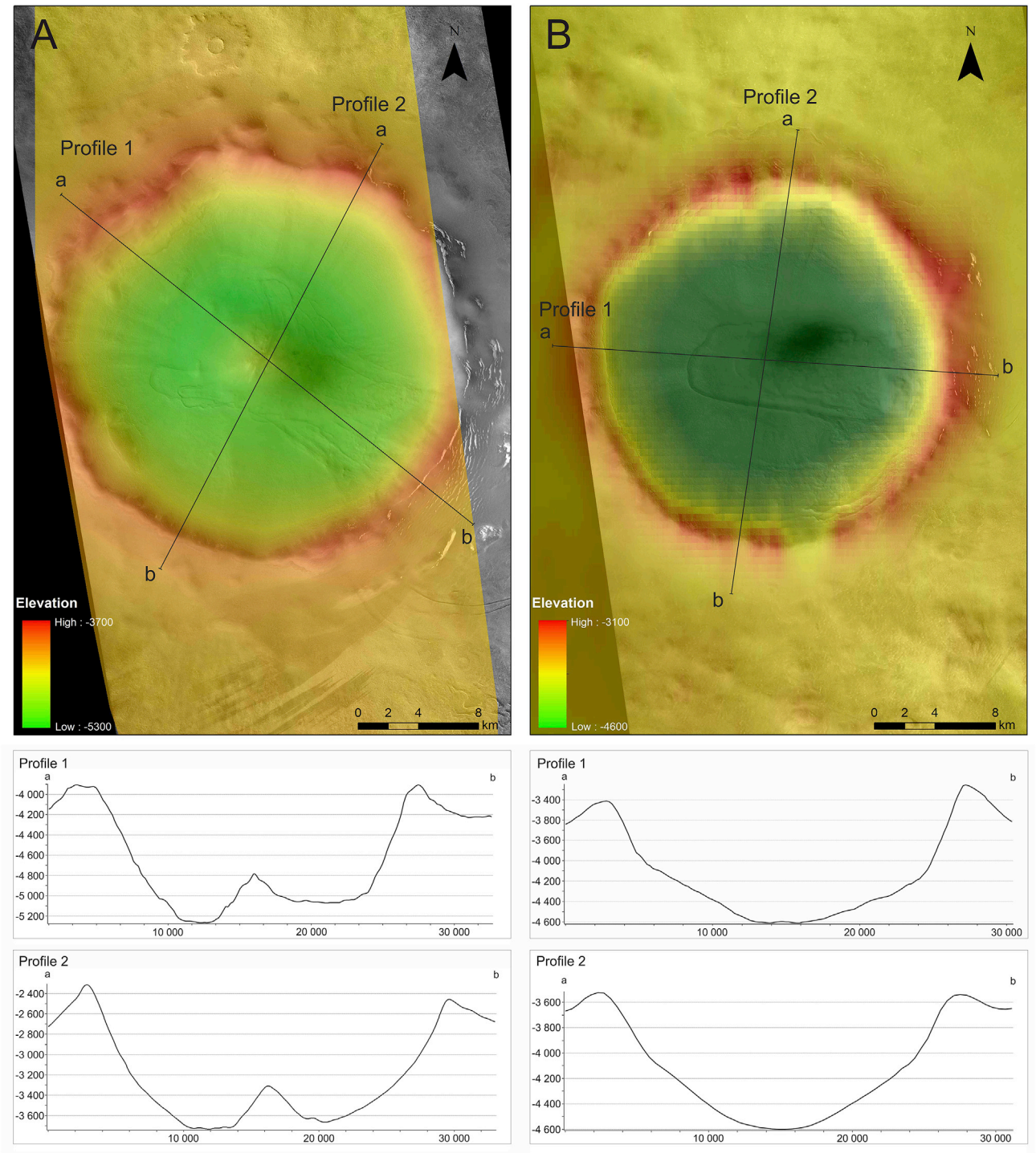

Fig. 1. Elevation maps of craters A and B and topographic profiles across the craters. For crater A, a DTM based on CTX stereopair images is shown. For crater B, MOLA data were used. Elevation is in meters. As a background, CTX images P22_009658_2505 (A) and D22_035807_2474 (B) are used.

et al., 1995; Tanaka et al., 2005), respectively. Crater A is 26.8 km in diameter (Garvin et al., 2006) and has a central peak. Crater B is 24 km in diameter and has a bowl shape (Fig. 1). Crater B has a more eroded rim, and the outer and inner slopes have down-slope mass wasting material transfer, like creep or solifluction. On the inner slopes of crater B is a well-exposed layered structure of regolith, which could suggest that this crater was once covered by a layered ice massif (Krasilnikov et al., 2018).

2. Origin of LMLR

In this work, we suggest a long-distance ice avalanche or fast-running surge mechanism as the origin of these features. The studied LMLRs are morphologically similar to catastrophic down-slope movement of water ice/rock mass as glacial surges or ice avalanches on Earth, with comparable lobate ridge morphology and behavior of modeled avalanche flow.

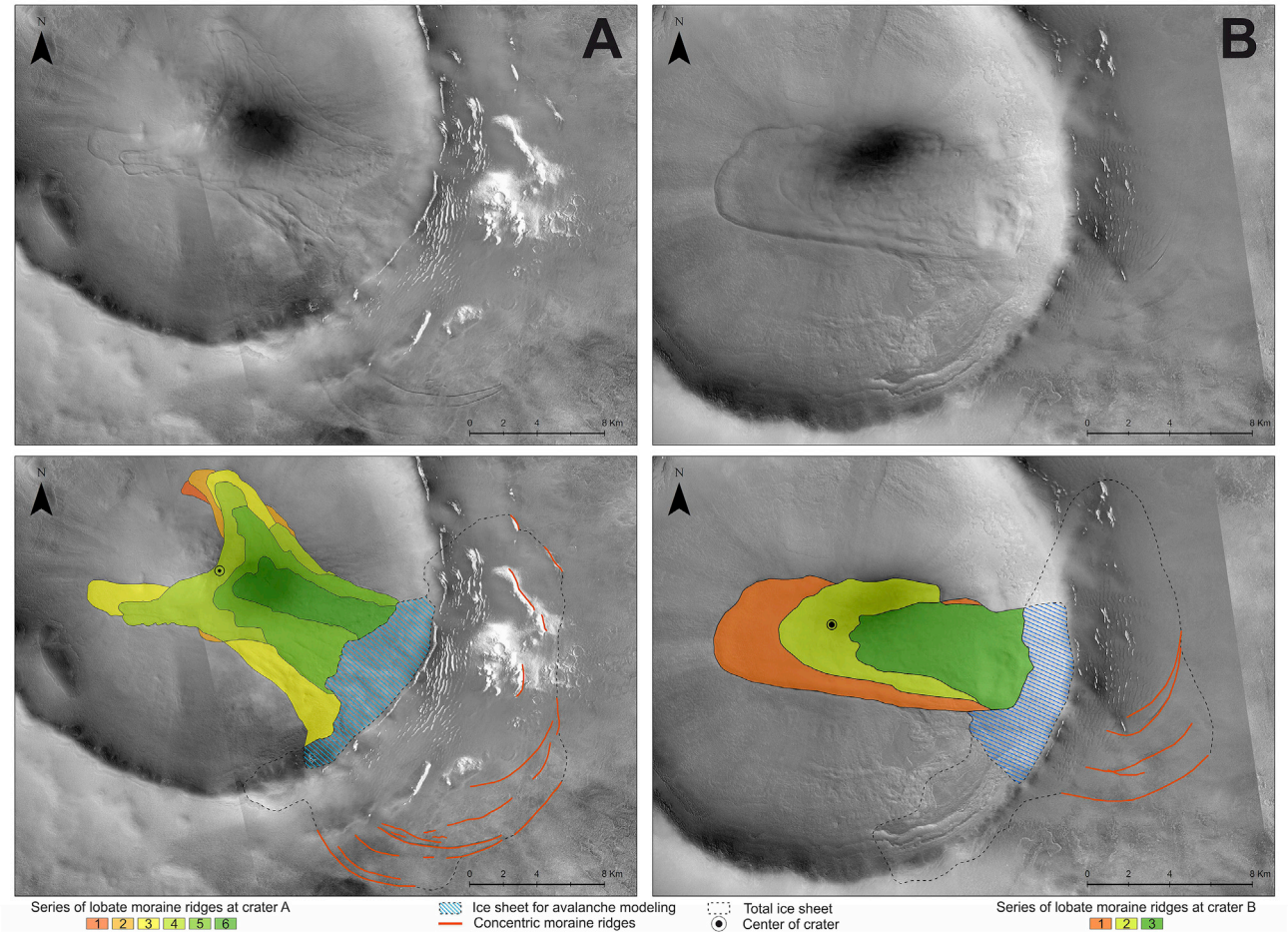

Fig. 2. Crater A (left) and crater B (right) with lobate moraine-like ridges (LMLR) on the inner slope and concentric moraine-like ridges (CMLR) on the outer slope. Six series in A and three well defined series in B of probable avalanche events are shown. CTX images B01_009935_2505 and D01_027644_2503 on A and D22_035807_2474 and G21_026537_2475 on B.

The main difference between the formation of an avalanche and that of the catastrophic down-slope movement of an ice massif (fast-running surge) is that down-slope movement occurs without the total destruction of the falling massif, whereas an avalanche is a combination of directional and random motion of flowing snow and ice granules. In this work, we focus on the avalanche formation hypothesis. The modeling of an ice avalanche under Mars' physical parameters (Fig. 5) produced a model similar to an avalanche model on Earth. For example, a potential analogue of this process is located in western Tibet, where a massive ice avalanche resulted from the collapse of two glaciers (Kääb et al., 2016). The second example is the 2002 Kolka Glacier event (Kazbek massif, Caucasus), where glacier instability lead to an ice/rock long-distance avalanche (Evans et al., 2009).

In the lower part of the avalanche flow, ice liquefaction from frictional heating may occur during collapse and downslope movement. This dynamic process could lead to the formation of LMLRs with well-defined lobate ridges. Below, we explain the hypothesis that LMLRs originate from ice avalanches.

In previous investigations, various hypotheses have been put forth regarding the formation of LMLRs. Garvin et al. (2006) showed that the origin of LMLRs in crater A could have a similar formation process to the typical drop moraines in terrestrial cold-based glacial environments. The equilibrium of sublimation from the glacier front, as well as forward ice velocity, led to the accumulation of parallel ridges at the front of glacier. In the case of Mars, the LMLR features might represent the remnants of cold-based H_2O glacier sheets that formed as a result of water ice accumulation on the southeastern rim of the craters, which occurred due to localized environmental conditions like climate, slope morphology etc. In Garvin et al. (2006), the authors proposed that the cold-based water ice glacier flowed down the crater wall, climbed the central peak structure and was passively diverted by it, subsequently undergoing several phases of advance and retreat. In the later study by Kreslavsky and Head (2011), it was argued that, in the present day, water ice cannot flow at these latitudes because of Mars' low temperatures, but more than 20 million years ago (Laskar et al., 2004) a high planet spin axis obliquity $\geq 60^\circ$ would make this a possibility. Following this assumption, the LMLR features could be formed by the down-slope movement of viscoplastic flow from a carbon dioxide (CO_2) glacier. The formation of a CO_2 massif with ~400 m thickness would be possible only at low planet obliquity values (Kreslavsky and Head, 2011). A glacial origin of lobate ridges is possible, however it has several weaknesses:

(1) The presence of well-defined lateral moraines suggests that their origin is related to dynamic processes. If we assume viscoplastic flow as can be observed in glaciers on Earth, the formation of lateral moraines occurs in two ways (Bennet and Glasser, 2009). The first is the migration of material to the border of the glacier from the surrounding territory of the valley, with typical slopes of 10°–40° (Bennet and Glasser, 2009). The second way formation could occur is through the partial ablation of the sides of the glacier and the subsequent accumulation of material inside (Bennet and Glasser, 2009). The first process would be possible on the upper part of the slope, where the slope is $> 10^\circ$, however in our case, the greatest concentration of LMLRs are located on

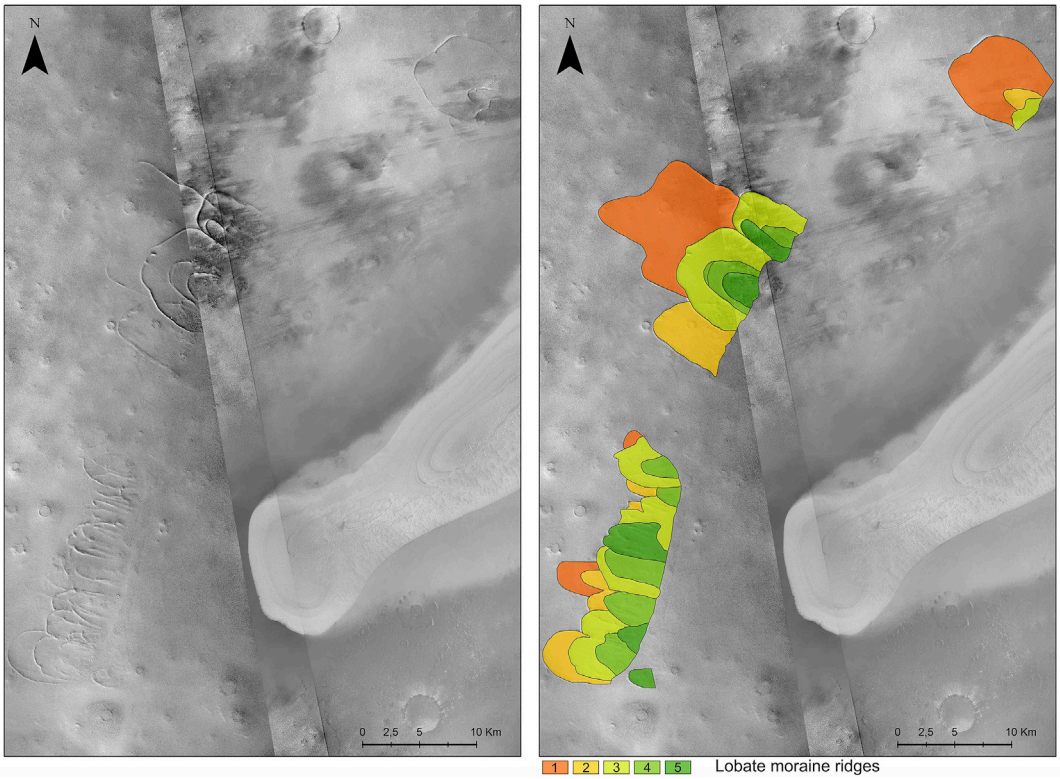

Fig. 3. Lobate moraine-like ridges (LMLR) on the northern plain near massif of ice layered deposits (74°N 95°E). Mosaic of CTX images P22_009717_2543, P16_007212_2539 and P21_009084_2541.

surface with slopes <8°. The formation of side moraine as a result of ablation is also unlikely, because this necessitates a dynamic glacial system with the active accumulation and ablation of material where only a few series of moraine exist. The formation of such features could also not occur in only a few periods of CO_2 rejuvenation under low obliquity. Significant lateral moraines thus represent the results of catastrophic down-slope movement of a high-volume massif.

(2) On a surface with a low slope (1°–8° for our craters' base), viscoplastic glacier flow would spread when glacier comes from the narrow valley to the plain, as happens on Earth. In our case, the directional movement of the material, with initial momentum and speed, allows the flow to cross the crater bottom and climb the opposite side of the inner crater rim (Fig. 1). The same scenario of fast directional flow can be applied to the formation of LMLR on the plain, at the site where C. Kreslavsky and Head (2011) mentioned that viscoplastic flow of CO_2 is less linear than H_2O flow, which could be case of lobate shaped ridge formation. Our assumption is that elongated lobate ridges could be formed through catastrophic downslope movement processes with initial momentum and speed, like an ice avalanche or fast-running surge;

(3) Under lower temperature conditions, H_2O is the first gas to condense, followed by CO_2. By virtue of western atmospheric mass transfer, this should occur first on slopes with western exposure. In Kreslavsky and Head (2005), atmospheric modeling under low obliquity showed the condensation of CO_2 and formation of perennial deposits on north-facing slopes. However, we observed deposits on slopes with northwestern or western exposure.

In the recent climatic epoch, on the outer southeastern and eastern slopes of the craters, local fields of H_2O frost are preserved during spring and summer (Fig. 2). These local frost deposits could point to the presence of water ice sheets on the craters' rim in past climate epochs;

(4) If we assume that the ridges in site C and the LMLRs in the craters have the same formation mechanism and source material, we should be able to identify the source of their formation. As the ridges are located on a flat surface, their source should be identifiable on a nearby inclined surface, where downslope movement could be initiated. The nearest slopes of ice layered deposits are located at a distance of ~20 km from the ridges and this could be the site where the massif formed and began to move. If so, it is probable that this massif occupied a larger territory in the period of the ridges' formation and its size later decreased due to sublimation (Kreslavsky and Head, 2011; Krasilnikov et al., 2018). Over-deposition of snow and ice on the slope of the ice massif would have led to an ice long-distance avalanche. Because the morphology of these ridges is similar to that of the LMLR, they were probably also formed by the same catastrophic down-slope movement of ice from the slopes of the parent body.

Additionally, there is a suggestion that LMLRs could be formed by viscoplastic flow of SO_2 solid phase deposits (Kreslavsky and Head, 2007). The process through which a large sulfur dioxide massif could form is not clear, and could have happened only in an epoch of vast and active volcanism. The last widespread volcanic eruptions on Mars happened in the Martian highlands near 20–50 million years ago (Werner, 2009), which exceeds the apparent age of LMLRs, based on their state of preservation.

In the present and recent climate, there have been two states of H_2O typical for Mars – vapor and solid form (ice). On Mars there are four types of features proposed to have formed due to viscoplastic flow of H_2O ice: lineated valley fill (LVF) (Squyres, 1978; Lucchitta, 1984), lobate debris aprons (LDA) (Baker et al., 2010; Head et al., 2010), viscous flow features (VFF) (Milliken et al., 2003) and tropical mountain glaciers (TMG) (Head and Marchant, 2003; Shean et al., 2005). These features are likely related to the movements of rock-ice mixtures on inclined surfaces, potentially similar to rock-glaciers on the Earth. The surface of these features is

covered by systems of longitudinal ridges, the morphology of which is very different from the morphology of LMLRs. In the northern plains, many mid-to large-sized craters with concentric crater fill (CCF) were discovered. These features are formed when a crater is filled by water ice deposits, which then undergo gradual degradation due to climatic changes (e.g. Kreslavsky and Head, 2006; Levy et al., 2010).

Variability in planetary spin axis obliquity wields a major influence on the composition and density of the atmosphere and presence of water ice on the surface. In the last 5 million years, obliquity has remained below 40°. Under low obliquity (<20°), the maximum solar radiation occurs at the equator and significant amounts of atmospheric water vapor condense at high latitudes (Forget et al., 2017). On the plain and in the craters around the NPLD, water ice layered massifs were formed and the northern polar cap spread to the lower latitudes (Krasilnikov et al., 2018). During periods with ~27°–35° obliquity, contrasts between the temperatures of the northern and southern hemisphere are significant, the atmosphere becomes more turbulent, and water ice begins to sublimate in polar regions, accumulating in the mid-latitudes of the highland zones. A large amount of CO_2 formed the seasonal polar caps (Forget et al., 2017) during this period. Several NPLD accumulation periods in the last 3 million years have been classified by Smith et al. (2016) based on radar SHARAD data analysis. The periods 0.37–2.1 Ma and 2.9–4.1 Ma, with high amplitude of planetary obliquity (between 15° and 35° (Laskar et al., 2004)), likely had low accumulation rates of ice material (Smith et al., 2016), but these periods are more suitable for of the expansion of the northern polar cap to the lower latitudes and the formation of water ice massifs (Krasilnikov et al., 2018). During periods 0–0.37 Ma and 2.1–2.9 Ma, the amplitude of spin axis obliquity changes was small (between 20° and 30°) (Laskar et al., 2004). In this period, ice at the low latitudes would have begun to sublimate and accumulation of ice most likely occurred in the polar cap regions (Smith et al., 2016).

The last period with high obliquity amplitude can be subdivided to the sub-periods 0.37–1.3 Ma and 1.3–2.1 Ma, both of which have similar values of obliquity amplitude. In these sub-periods, there were multiple instances in which obliquity values decreased to below 20°. This led to a temperature decrease in the polar regions and the formation of separate ice massifs in the northern polar region. The active formation of the NPLD deposits – together with the shifting of the NPLD edge towards lower latitudes during the period of 0.37–2.1 Ma – promoted the formation of isolated water ice massifs in the ~60°–70° northern latitudes (Head et al., 2003; Forget et al., 2017; Krasilnikov et al., 2018). We assume that the studied objects were formed in the 0.37–1.3 Ma sub-period under cycles with low obliquity (15°–20°). As a result of low concentrations of H_2O in the atmosphere of Mars, its condensation primarily occurred on slopes with western exposures (Head and Marchant, 2003), reflecting the western transfer of air masses (www-mars.lmd.jussieu.fr). Formation of both ice massifs (as glaciers) on the eastern part of craters A and B and ice massifs on the northern plain (site C) could have occurred in this period. The excessive accumulation of ice on the inclined surfaces, such as on the slopes of craters or the slopes of ice massifs on the northern plain, could provoke the catastrophic down-slope movement of unstable parts of H_2O ice massifs, resulting in the formation of LMLR features.

The observed position of LMLR and CMLR features in the southeastern part of the craters suggests that these types of ridges were formed through ice mass down-slope movement from both sides of the crater's rim from a single per crater glacier sheet. The western part of the glacier was located on the inner steep slope of the crater, while its eastern part was situated on the outer gently sloping surface. Therefore, on the steep, inner slope, catastrophic disruptions of the ice mass (like glacier surge or ice avalanche) could occur periodically and cause the formation of LMLRs. The overlapping nature of the ridges indicates multiple episodes of glacial advance and retreat. A different situation can be observed on the outer gentler slope, where a glacier should have slow viscoplastic down-slope movement that resulted in CMLR formation (like frontal moraines). However, according to Kreslavsky and Head (2011), the temperature conditions in recent times do not allow for the viscoplastic flow of water ice.

In order to test our hypothesis about the origin of LMLR, we conducted modeling of down-slope movement of an ice avalanche on the crater's inner slope, provoked by the breakdown of an ice mass from a glacier sheet located on the crater's rim.

3. Modeling of ice long distance avalanche

To calculate the down-slope movement of the ice massif, two different approaches were used. First, the modeling of an avalanche in Rapid Mass Movement Simulation (RAMMS) (Christen et al., 2010) was conducted. This software was developed for modeling gravitational processes, such as avalanches, debris flow, landslides and rockfalls. In this work, the RAMMS:AVALANCHE (Christen et al., 2010) module was used. Second, we checked our RAMMS modeling results for the calculation of an avalanche or fast ice down-slope movement using a graph-analytical method (Kozik, 1962), which includes estimating avalanche velocity and maximum distance.

3.1. Data for the numerical calculation of ice massif down-slope movement

As a topographic base for modeling, a digital terrain model (DTM) (Fig. 4) based on CTX stereo images (~6 m/pix resolution (Malin et al., 2007)) was used for crater A (Krasilnikov et al., 2017). In this instance, radiometric correction of images P22_009658_2505 and B01_009935_2505 was conducted. Images were co-registered using 15 tie points and adjusted using a rational polynomial coefficient (Zubarev et al., 2016) in PHOTOMOD 6.0 software (Adrov et al., 1995). The total root-mean-square error is 0.4 pixel on images and the vertical accuracy is 15 m.

The area of the fallen massif of water ice was estimated using CTX images (Fig. 2) and is equal to ~32.1 km^2 for crater A. The area under avalanche influence is about 104 km^2, which was measured using CTX images and located inside the moraine-like ridges. This area has been disturbed by an avalanche stream and subsequently covered by avalanche deposits. The maximum distance (L) covered by the avalanche is ~14–15 km, with a maximum width of 5 km. The difference in elevation (H) from start to end points is about 1.3 km. The ratio of H/L is 0.09, which corresponds to long distance avalanches (<0.6) on Earth (Scheidegger, 1975; Dade and Huppert, 1998). For our terrestrial examples in western Tibet (Kääb et al., 2016) and in the northern Caucasus (Evans et al., 2009), the ratio of H/L is about 0.05 and 0.07 respectively.

The area of the fallen massif of ice in crater B is about 21.1 km^2, while the area under avalanche influence is ~78.4 km^2. The maximum distance is (L) ~13–15.5 km with a maximum width 5.5 km. The difference in elevation is (H) ~1.1 km. The ratio of H/L is 0.08, which again corresponds to long distance avalanches in terrestrial environments. The thickness of the original ice massifs of 100 and 500 m (as mentioned previously, the thickness of the ice deposit near site C is about 400 m in height at the present time) was chosen for modeling of avalanche in RAMMS software.

With the assumption that the formation of ice layered deposits around the north polar cap happened in the same time period as formation of NPLD (e.g. Smith et al., 2016), the physical parameters (such as the density etc.) should be the same (Krasilnikov et al., 2018). The calculation of the density of the modeled ice massifs is based on the composition of components (silicate dust ~30% and 70% ice) of polar layered deposits (Cull et al., 2010; Brown et al., 2012), yielding a density of about 1.01 g/cm^3.

3.2. Modeling in RAMMS::AVALANCHE

An avalanche is hypothesized as one of possible processes through which LMLRs were formed, as the result of a combination of directional and random motion of flowing snow and ice granules.

RAMMS:AVALANCHE software was designed by Institute for Snow and Avalanche Research SLF for avalanche engineers to map hazards.

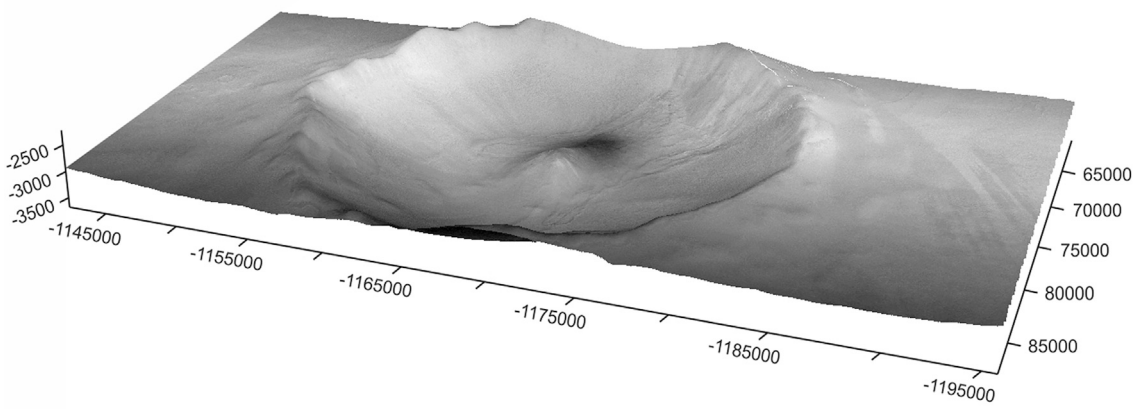

Fig. 4. Digital elevation model of the crater A based on CTX images P22_009658_2505 and B01_009935_2505.

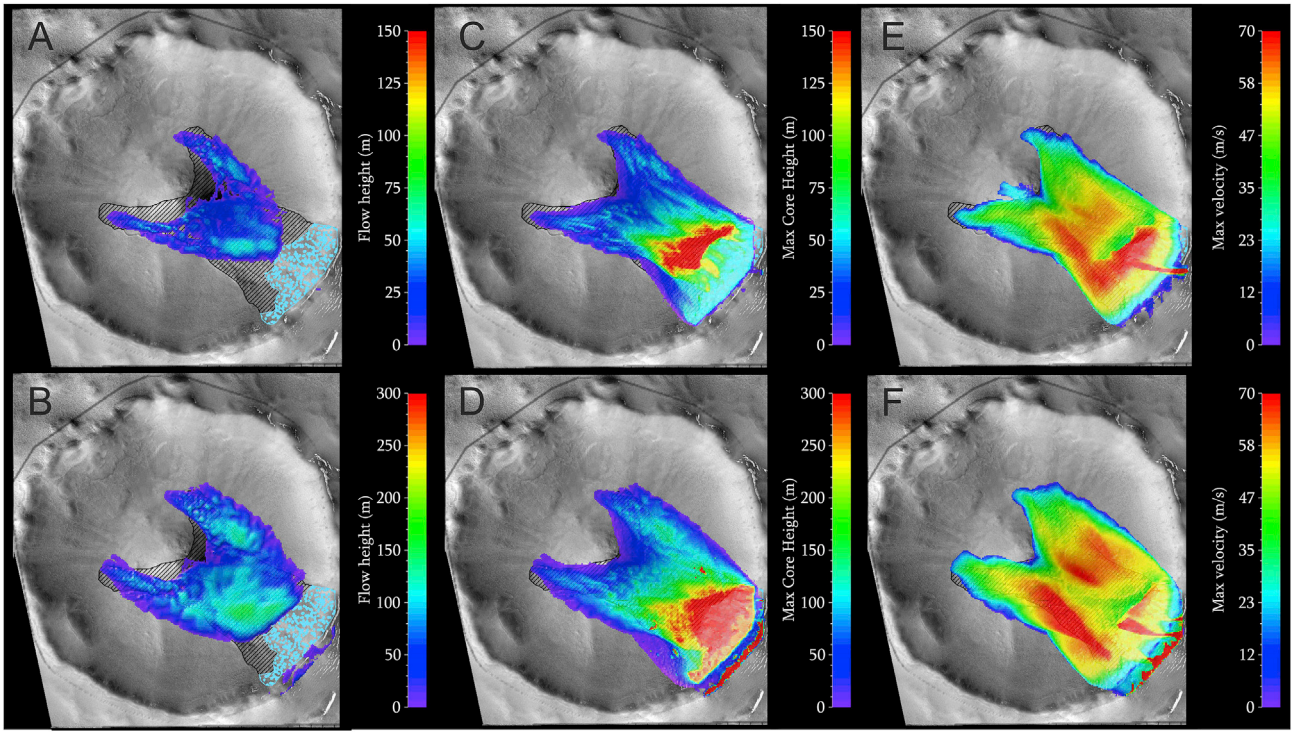

Fig. 5. Results of surge modeling with RAMMS:AVALANCHE on the inner slope of crater A with initial ice thickness of 100 m (A, C, E) and 500 m (B, D, F). A and B, the final thickness of ice deposits after avalanche. C and D, the maximum core (main massif) thickness during the entire simulation. E and F, the maximum speed during the entire simulation.

This program models the movement of a snow stream in three-dimensional terrain. The modeling allows the user to determine zones affected by avalanche and analyze the stream's evolution over time. Furthermore, two types of approaches can be applied: the standard Voellmy–Salm (VS) (Salm, 1993) approach or a random kinetic energy (RKE) model (Bartelt et al., 2006). The VS approach includes two parameters (volume and speed) to calculate impact pressure. This model works poorly with snow cover entrainment and only allows for the calculation of maximum flow heights and velocities at the head of avalanche, as well as avalanche runout distances. In our study, the more complicated RKE approach was used. This approach includes an additional flow model based on the production, transport and decay of the kinetic energy of random motion associated with the mass of flowing snow and ice granules (Bartelt et al., 2012, 2014).

In the RKE approach, the calculation of avalanche flow is realized in a three-dimensional environment, which allows us to set important parameters for modeling, such as volume and direction of flow. Using variable parameters, different physical properties, including atmosphere pressure (P) and temperature (T) in the studied area, can be set and adjusted to Mars' physical parameters. Climatic parameters for modeling were calculated using average values for the winter season in this region of Mars Climate Database v5.2 (www-mars.lmd.jussieu.fr). The annual mean atmosphere pressure in the studied area is 830 Pa, with a surface temperature of −90 C° and Mars' gravity of 3.77 m/s^2. The maximum distance of the avalanche was measured by measuring LMLRs' borders on the images. Then, the thickness of the original ice massif was calculated, with massif thicknesses being gradually increased until the end point of modeled avalanche reached the observed boundaries of LMLRs.

We assumed that the type of modeled avalanche would be close to the terrestrial snow-ice type of avalanche, but with some content of silicate

material (~5–30%). Shear deformation of the ice base layer occurs due to the decoupling of differently composed and structured ice massif layers. A possible reason for the disruption between ice layers could be an exceedance of the threshold value of shear stress on the base layer as a result of over deposition of ice on the inclined surface.

For our goals, corrections to the physical parameters of the "avalanche" module were made. The models were made for two thicknesses of the original massif – 100 and 500 m (the first and the second experiment below) (Fig. 5). We focused on a few different parameters of the avalanche process. The major parameter was the maximum distance covered by an avalanche. It was very important that the end moraines in the studied crater and the maximum distance of modeled avalanche matched. Increasing the initial thickness of the ice sheet on the slope within the model, we produced longer-distance avalanches. Having increased the thickness until the front of avalanche reaches the LMLR, we are able to estimate the original thickness of the massif. Using data of the maximum speed of an avalanche stream, we can compare the results with the modeling of the ice massif down-slope movement by graph-analytical approach.

The modeled maximum speed of an avalanche in the end of the steep slope reached 50–70 m/s (Fig. 5). The deceleration of the avalanche is better represented by the first experiment. After reaching the bottom of the crater, the speed of the avalanche decreases to 35 m/s in the first experiment, while the momentum of the stream in the second experiment allows for the preservation of stream dynamics, maintaining speed at 60 m/s. The central peak had a significant effect on the resulting shape of the stream. A central peak with ~200 m height divides the stream in two parts in both experiments. In these experiments, the stream reached the top of the peak, irrespective of thickness of original massif. In the first experiment, the front of the avalanche fell short of the end moraines, but in the second experiment it covered the main area of the crater bottom and crossed the end/lateral moraines. After two series of modeling, the results were extrapolated and it was determined that the original H_2O ice deposits had a thickness of ~200 m.

3.3. Graph-analytical method, estimation of highest velocity and the distance limit of an avalanche

An evaluation of the velocity and maximum distance of the avalanche can be conducted using the graph-analytical method (Kozik, 1962). This method includes analytical and graphical approaches. In the analytical approach, the profile is divided into almost linear segments and the number of segments depend on the accuracy of measurement. The segments are characterized by their projected length, height (Δx_i, Δy_i), inclination $a_i = a\tan(\Delta y_i/\Delta x_i)$ and segment length $s_i = \sqrt{\Delta x_i^2 + \Delta y_i^2}$. Kozik (1962) suggested the use of the movement of the mass point on the inclined surface for the approximate calculation of avalanche velocities. This method conceives of this process as a movement of an avalanche on an inclined surface with the mass remaining constant during its motion (Voitkovskiy, 1999). In this case, avalanche movement mainly depends on three factors: gravity, friction force (described by Colomb's law) and environmental resistance (directly proportional square of velocity). Environmental resistance is affected by the roughness of the underlying surface, the air pressure on the front line of the avalanche etc.

Following Kozik (1962), we used a differential equation:

$$\frac{\partial(v^2)}{\partial s} = 2\left(a - bv^2\right) \tag{1}$$

where the initial condition $v_0 = 0$ (moment of avalanche separation), $a = g(\sin a - f\cos a)$, v is speed, g is gravity, f is friction coefficient, $b = q/M$, q is mass of objects per unit of length located in the path of the avalanche and M is mass of avalanche.

Following Kozik (1962), the environmental resistance is not significant in comparison to the friction force. Therefore, we assume that $b = 0$, then the previous equation (1) has the form:

$$\frac{\partial(v^2)}{\partial s} = 2a. \tag{2}$$

After the integration of (2) with the initial speed $v_0 = 0$, we have the solution:

$$v^2 = v_0^2 + 2g(\sin a - f\cos a)s \tag{3}$$

In order to calculate the highest avalanche speed, it is necessary to let $f = r_{min}$. The value of the minimum friction coefficient (r_{min}) is constant for the whole profile. Computation is consequently conducted for each segment using (3), beginning from the first segment by $v_0 = 0$. Then, using parameters of the segment: inclination α_1, length of segment s_1, Mars' gravity (3.77 m/s^2) and r_{min}, we calculate the velocity of the avalanche front v in the end of this segment. Then this value is used as the starting velocity in the second segment and so on.

The graphical approach was used for the purpose of checking the analytical results. A graphical approach allows for the estimate of the highest velocity in any given point (x, y) of profile avalanche movement. Velocity can be calculated as (Kozik,1962):

$$\frac{v^2}{2g} = y - r_{min}x \tag{4}$$

The right part of (4) is a graphic interval that is numerically equal to the distance between y(x) (profile elevation) and straight line $y1(x) = r_{min}x$ passing through point (0, 0). Velocity can be calculated from (5):

$$v = \sqrt{2g(y - r_{min}x)} \tag{5}$$

There are two variants of the considered avalanches: when H and L – are known and when L is unknown beforehand.

1. If the height of avalanche separation (H) and runout (L) are known, then $r_{min} = H/L$ and $v = \sqrt{2g(y - r_{min}x)}$. Using analytic geometry, we calculate velocity (5) instead of drawing a straight line and defining the difference between the profile and straight line. This approach was used for the computation of avalanche speed in our case.
2. There is height (H), but avalanche runout (L) is unknown beforehand. It is necessary to predict length of possible L depend of given height of separation (H). In definition of L, r_{min} is used. According Kozik (1962), for the Earth $r_{min} = 0.3$ and $L = H/r_{min}$ or $L = 3.3H$.

For these computations, profiles in craters A and B (image 1, A and B correspondingly) were used. In crater A, the profile was based on CTX DEM data and for crater B, on MOLA data. For crater A, we computed two scenarios of avalanches, one with an end point on the central crater peak and the other with an end point with the maximum distance at the end of left branch. The value of r_{min} for our craters was calculated from the H to L ratio and consequently have similar values ~0.07 and ~0.06 for A and B crater respectively. This r_{min} exhibits a small difference to previous estimations of H/L for both craters (0.09 and 0.08 for craters A and B respectively), due to measurement error in the graphical approach and the influences of Mars' environment.

Finally, we compared these results with the more complicated random kinetic energy method and found approximately the same results for the predicted avalanche speed (Fig. 6). The RAMMS model reflects relief variations much better, as is shown by the reaction of speed flow on the slope inclination, with changes near $x = 4200\ m$ at Fig. 6 (a) and $x = 4500\ m$ at Fig. 6 (b). On the low-incline surface, both models have similar values.

We suggest that LMLR on the plain (site C) were also formed by the catastrophic down-slope movement of an ice avalanche, but in this case, ice movement occurred from the slope of an ice massif. Using the graph-analytical method, we can calculate the approximate thickness and length of the ice massif in that period, when its edge was located at the

point where the LMLR begin. The first part of a modeled avalanche was located on the slope of the massif and the second on the plain. The avalanche runway was divided into four parts, with three segments on the ice massif slope and one segment on the plain. The distance of the avalanche on the plain was measured as the mean length of LMLR (~6 km) with a clearly recognizable beginning point. Using the graphical approach, the friction coefficient can be calculated as $\tan a = r_{min}$. The value of the friction coefficient for the main plain model was set as ~0.06.

With a small variation of friction (dependent on tan *a*), several models of the probable parameters of the ice massif were made (Fig. 7). The modeled avalanche detaches from point D, accelerates until point B, passes onto the flat surface, and moves up to stop at point C (Fig. 7). The height in these models varied from ~480 m to ~780 m (AD). Depending on the height and friction coefficient, the corresponding length varied from ~600 m to ~4600 m (AB). The modeled ice deposit slope in these models varied from ~40°–9°. The current ice layered massifs near the studied area have a slope of ~6° and are ~400 m thick. Our modeled massif should be thicker and have a steeper slope, but not one that is substantially steeper. Finally, after a series of models, we decided the most probable massif height of ~600 m, with a 2000 m slope length (Fig. 7). With these parameters, average slope was ~17°.

4. Conclusions

At the high northern latitudes of Mars, there are two impact craters (70.3°N 266.45°E (A) and 67.25°N 249.45°E (B)) with lobate moraine-like ridges (LMLR) on the eastern inner slopes (Fig. 2). On the northern plain (74°N 95°E, site C), to the northwest of the layered ice massif, ridges with similar morphology and morphometric parameters were found (Fig. 3). We suggest that these LMLR were formed by long-distance ice avalanches. On the other hand, on the outer eastern slopes of the craters, concentric moraine-like ridges (CMLR) were observed. The formation of these cannot be explained by long-distance ice avalanches, but were instead probably the result of H_2O ice fast-running surges. The formation of a surge on the outer slope could have occurred in the same time period as an avalanche and does not contradict our thesis.

Long distance avalanches are formed when the threshold shear stress on the base layer is overcome. This variation of ice massif thickness would have occurred in a short period and only a few times, and this would lead to the formation of a series of LMLR. Overdeposition of the ice at high latitudes could have happened only under the low planetary spin axis obliquity (<20°) (Head et al., 2003; Forget et al., 2017). The formation of water ice massifs on the studied latitudes could have occurred in the last climatic period, with the shifting of the NPLD edge to lower latitudes (0.37–1.3 Ma). This suggestion is consistent with the age estimation for LMLR made by Kreslavsky and Head (2011), when they assumed these features had a glacial origin and that their approximate age was 0.6–0.8 Ma for the youngest and 2–3 Ma for the oldest series. In this period, the climate situation and local meteorology allowed massifs of water ice with ~200 m thickness to form on the eastern rim of crater A and crater B. The avalanches formed six series of LMLR in crater A and three series in crater B. RAMMS and graph-analytical models of the flow yield approximately the same speed values.

After two series of modeling using RAMMS software, it was decided that initial H_2O water ice deposit in crater A would have had ~200 m thickness (slightly thicker than the modeled 100 m thickness). For the avalanche modeling in crater B, a graph-analytical approach was used. This method cannot estimate thicknesses ice massif, but does provide the front speed of the avalanche. The calculated avalanche speed in crater B is approximately the same as in crater A. The absence of a central peak in this crater, together with the number and morphology of LMLR, allow us to suggest that the thickness of the original ice massif on the crater rim of crater B is equal to the modeled deposit in crater A: ~100–150 m.

On the plain with 74°N 95°E coordinates, an ice massif (with ~400 m thickness) and LMLR to the northwest at a distance of ~10–20 km was observed. We assume that this ice massif was historically spread over a bigger territory and on these slopes a long-distance ice avalanche formed. Using the graph-analytical method, the morphometric parameters of the original ice massif were calculated. The most probable parameters of modeled massif are ~600 m in height and 2 000 m of slope width (Fig. 7), with surface friction force set as ~0.06.

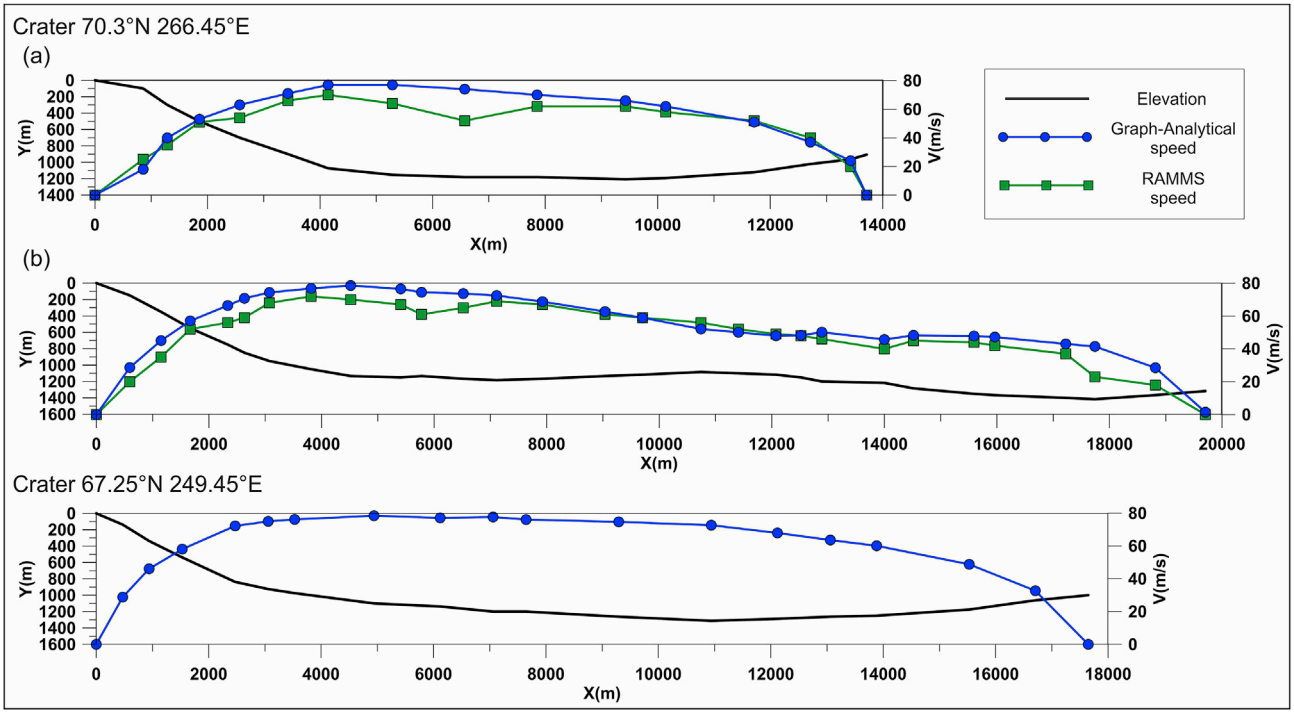

Fig. 6. Speed profiles of avalanches in crater A with central peak (a) and without central peak (b), using Graph-analytical method (dots) and random kinetic energy method calculated by RAMMS (squares). Graph-analytical computation of avalanche speed in crater B below.

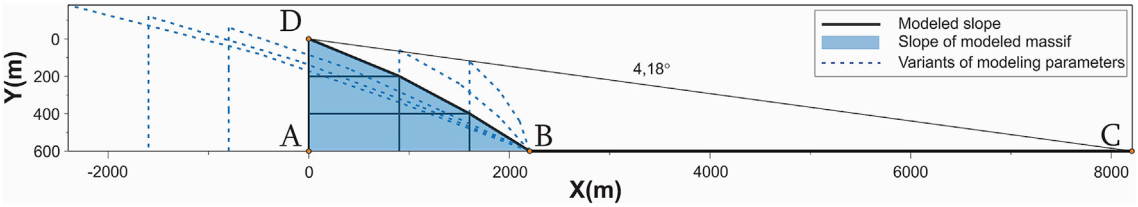

Fig. 7. The modeling of an ice massif on the plain (site C) using the graph-analytical method. Few variants of potential massif were calculated (dotted line) and most probable parameters of the slope were chosen. Solid bold line shows the runway of avalanche in the beginning of massif slope (point D) and with the end point on the plain (point C). $AC = L$ and $AD = H$, AB, base of the massif.

In this paper, the formation of long-distance ice avalanches or fast-running surges at the high northern latitudes of Mars under low obliquity are hypothesized. We assumed that this downslope movement formed lobate moraine-like ridges (LMLR) in two craters 70.3°N 266.45°E (A), 67.25°N 249.45°E (B) and on the plain 74°N 95°E, site C. Modeling of ice avalanches was conducted. The two types of models used produced similar results. These models allow us to estimate speed (max ~80 m/s) and the original thickness of the ice massif in crater A (~150 m) and on the plain (~600 m) where the avalanches formed. The results of the modeling conducted conform with the suggested hypothesis of LMLRs' formation by long-distance ice avalanche. The formation of the studied features relates to the shifting of NPLD borders to the south (~70°) and the formation of ice layered massifs up to 60° in relatively recent history (0.37–1.3 Ma years ago). In the present period (0–0.37 Ma) the studied massifs were partly sublimated (~200 m of ice was lost, which applies to all three studied places). Water ice was preserved as local fields of frost on the outer southeastern and eastern slopes of the craters, which could be remnants of ice deposits in past climate epochs. The partly sublimated ice layered deposit at site C (74°N 95°E) would have been spread over a bigger territory in the historical period and on these slopes a long-distance ice avalanche formed.

Declaration of competing interest

This paper "Krasilnikov S.S., Kuzmin R.O., Bühler Y., Zabalueva E.V. Formation of long-distance water ice avalanches on Mars" have no conflict of interest.

All funding sources have been acknowledged. This manuscript or a very similar manuscript has not been published, nor is under consideration by any other journal.

All authors agree with the contents of the manuscript and its submission to the journal. All authors listed have contributed significantly to the work and agree to be in the author list.

CRediT authorship contribution statement

S.S. Krasilnikov: Conceptualization, Methodology, Validation, Resources, Writing - original draft, Visualization, Project administration. **R.O. Kuzmin:** Conceptualization, Writing - review & editing. **Y. Bühler:** Methodology, Software, Visualization. **E.V. Zabalueva:** Methodology, Writing - review & editing.

Acknowledgments

KSS partly supported by Deutscher Akademischer Austauschdienst. The authors appreciate the assistance of D. Brazier.

References

Adrov, V.N., Chekurin, A.D., Sechin, A.Yu, Smirnov, A.N., Adam-Guillaume, J.-P., Quessete, J.-P., 1995. Program PHOTOMOD: digital photogrammetry and stereoscopic image synthesis on a personal computer. Proc. SPIE 2646, 89–96. https://doi.org/10.1117/12.227853.

Baker, D.M.H., Head, J.W., Marchant, D.R., 2010. Flow patterns of lobate debris aprons and lineated valley fill north of Ismeniae Fossae, Mars: evidence for extensive mid-latitude glaciation in the Late Amazonian. Icarus 207, 186–209. https://doi.org/10.1016/j.icarus.2009.11.017.

Bartelt, P., Bühler, Y., Buser, O., Christen, M., Meier, L., 2012. Modeling mass-dependent flow regime transitions to predict the stopping and depositional behavior of snow avalanches. J. Geophys. Res.: Earth Surface 117 (November 2011), 1–28. https://doi.org/10.1029/2010JF001957.

Bartelt, P., Buser, O., Platzer, K., 2006. Fluctuation–dissipation relations for granular snow avalanches. J. Glaciol. 52, 631–643. https://doi.org/10.3189/172756506781828476.

Bartelt, P., Buser, O., Buehler, Y., Dreier, L., Christen, M., Hicks, M., Brinkgreve, R., Rohe, A., 2014. Numerical Simulation of Snow Avalanches: Modelling Dilatative Processes with Cohesion in Rapid Granular Shear Flows, Numerical Methods in Geotechnical Engineering. Taylor & Francis Group, London, pp. 327–332.

Bennet, M., Glasser, N., 2009. Glacial Geology. Ice Sheets and Landforms. Wiley-Blackwell, London.

Brown, A.J., Calvin, W.M., Murchie, S.L., 2012. Compact Reconnaissance Imaging Spectrometer for Mars (CRISM) north polar springtime recession mapping: first 3 Mars years of observations. J. Geophys. Res.: Plan 117, E00J20. https://doi.org/10.1029/2012JE004113.

Christen, M., Kowalski, J., Bartelt, P., 2010. RAMMS: numerical simulation of dense snow avalanches in three-dimensional terrain. Cold Reg. Sci. Technol. 63, 1–14. https://doi.org/10.1016/j.coldregions.2010.04.005.

Cull, S., Arvidson, R.E., Morris, R.V., Wolff, M., Mellon, M.T., Lemmon, M.T., 2010. Seasonal ice cycle at the Mars Phoenix Landing Site: 2. postlanding CRISM and ground observations. J. Geophys. Res. 115, E00E19. https://doi.org/10.1029/2009JE003410.

Dade, W.B., Huppert, H.E., 1998. Long-runout rockfalls. Geology 26, 803–806. https://doi.org/10.1130/0091-7613(1998)026<0803:LRR>2.3.CO;2.

Evans G., S., Tutubalina V., O., Drobyshev N., V., Chernomorets S., S., McDougall, S., Petrakov A., D., Hungr, O., 2009. Catastrophic detachment and high-velocity long-runout flow of Kolka Glacier, Caucasus Mountains, Russia in 2002. Geomorphology 105, 314–321. https://doi.org/10.1016/j.geomorph.2008.10.008.

Forget, F., Byrne, S., Head, J.W., Mischna, M.A., Schörghofer, N., 2017. Recent climate variations. In: Haberle, R.M., Clancy, R.T., Forget, Francois, Smith, M.D., Zurek, R.W. (Eds.), The Atmosphere and Climate of Mars. Cambridge University Press, Cambridge, pp. 497–525. https://doi.org/10.1017/9781139060172.016.

Garvin, J.B., Head, J.W., Marchant, D.R., Kreslavsky, M.A., 2006. High-latitude cold-based glacial deposits on Mars: multiple superposed drop moraines in a craterinterior at 70°N latitude. Meteoritics Planet Sci. 41, 1659–1674. https://doi.org/10.1111/j.1945-5100.2006.tb00443.x.

Head, J.W., Marchant, D.R., 2003. Cold-based mountain glaciers on mars: western arsia mons. Geology 31, 641–644. https://doi.org/10.1130/0091-7613(2003)031<0641:CMGOMW>2.0.CO;2.

Head, J.W., Marchant, D.R., Dickson, J.L., Kress, A.M., Baker, D.M., 2010. Northern mid-latitude glaciation in the Late Amazonian period of Mars: criteria for the recognition of debris-covered glacier and valley glacier landsystem deposits. Earth Planet Sci. Lett. 294, 306–320. https://doi.org/10.1016/j.epsl.2009.06.041.

Head, J.W., Mustard, J.F., Kreslavsky, M.A., Milliken, R.E., Marchant, D.R., 2003. Recent ice ages on Mars. Nature 426, 797–802.

Kääb, A., Leinss, S., Gilbert, A., Bühler, Y., Gascoin, S., Evans, S.G., Bartelt, P., Berthier, E., Brun, F., Chao, W.-A., Farinotti, D., Gimbert, F., Guo, W., Huggel, C., Kargel, J.S., Leonard, G.J., Tian, L., Treichler, D., Yao, T., 2016. Massive collapse of two glaciers in western Tibet in 2016 after surge-like instability. Nat. Geosci. 11 (2), 114–120. https://doi.org/10.1038/s41561-017-0039-7.

Kozik, S.M., 1962. Computing Snow Avalanche Motion. Gidrometeoizdat, Leningrad (In Russian).

Krasilnikov, S.S., Brusnikin, E.S., Zubarev, A.E., Bühler, Y., Kuzmin, R.O., 2017. Construction of a digital terrain model of Mars based on Context Camera (CTX) images for further geological and geomorphological analysis. Current problems in remote sensing of the Earth from space 14, 265–272.

Krasilnikov, S.S., Kuzmin, R.O., Evdokimova, N.A., 2018. Remnant massifs of layered deposits at high northern latitudes of Mars. Sol. Syst. Res. 52, 26–36.

Kreslavsky, M.A., Head, J.W., 2005. Mars at very low obliquity: atmospheric collapse and the fate of volatiles. Geophys. Res. Lett. 32, L12202. https://doi.org/10.1029/2005gl022645.

Kreslavsky, M.A., Head, J.W., 2006. Modification of impact craters in the northern plains of Mars: implications for Amazonian climate history. Meteoritics Planet Sci. 41 (10), 1633–1646. https://doi.org/10.1111/j.1945-5100.2006.tb00441.x.

Kreslavsky, M.A., Head, J.W., 2007. Unusual glacial-like features in the high-arctic of Mars. In: 38th Lunar Planet. Sci. Conf., Abs., p. 1576.

Kreslavsky, M.A., Head, J.W., 2011. Carbon dioxide glaciers on Mars: products of recent low obliquity epochs. Icarus 216, 111–115. https://doi.org/10.1016/j.icarus.2011.08.020.

Laskar, J., Correia, A.C.M., Gastineau, M., Joutel, F., Levrard, B., Robutel, P., 2004. Long term evolution and chaotic diffusion of the insolation quantities of Mars. Icarus 170, 343–364. https://doi.org/10.1016/j.icarus.2004.04.005.

Levy, J., Head, J.W., Marchant, D.R., 2010. Concentric crater fill in the northern mid-latitudes of Mars: formation processes and relationships to similar landforms of glacial origin. Icarus 209, 390–404. https://doi.org/10.1016/j.icarus.2010.03.036.

Lucchitta, B.K., 1984. Ice and debris in the fretted terrain, mars. J. Geophys. Res. 89, B409–B418. https://doi.org/10.1029/JB089iS02p0B409.

Malin, M.C., Bell, J.F., Cantor, B.A., Caplinger, M.A., Calvin, W.M., Clancy, R.T., Edgett, K.S., Edwards, L., Haberle, R.M., James, P.B., Lee, S.W., Ravine, M.A., Thomas, P.C., Wolff, M.J., 2007. Context camera investigation on board the mars reconnaissance orbiter. J. Geophys. Res.: Plan 112, 1–25. https://doi.org/10.1029/2006JE002808.

Milliken, R.E., Mustard, J.F., Goldsby, D.L., 2003. Viscous flow features on the surface of mars: observations from high-resolution mars orbiter camera (MOC) images. J. Geophys. Res. 108, E6. https://doi.org/10.1029/2002JE002005.

Salm, B., 1993. Flow, flow transition and runout distances of flowing avalanches. Ann. Glaciol. 18, 221–226. https://doi.org/10.3189/S0260305500011551.

Scheidegger, A.E., 1975. Physical Aspects of Natural Catastrophes. Elsevier Scientific Publishing, New York. https://doi.org/10.1002/eqe.4290040512.

Scott, D.H., Zimbelman, J.R., Dohm, J.M., 1995. 1:1 Million-Scale Geologic Maps of Mars' Tharsis Montes.

Shean, D.E., Head, J.W., Marchant, D.R., 2005. Origin and evolution of a cold-based tropical mountain glacier on Mars: the Pavonis Mons fan-shaped deposit. J. Geophys. Res. 110, E05001. https://doi.org/10.1029/2004JE002360.

Smith, I.B., Putzig, N.E., Phillips, R.J., Holt, J.W., 2016. An ice age recorded in the polar deposits of Mars. Science 352, 1075–1078.

Squyres, S.W., 1978. Martian fretted terrain: flow of erosional debris. Icarus 34, 600–613. https://doi.org/10.1016/0019-1035(78)90048-9.

Tanaka, K.L., Skinner, J.A., Hare, T.M., 2005. Geologic Map of the Northern Plains of Mars. U.S. Geological Survey Scientific Investigations Map 2888. Scale 1:15,000,000.

Voitkovskiy, K.F., 1999. Fundamentals of Glaciology. Nauka, Moscow (In Russian).

Werner, S.C., 2009. The global martian volcanic evolutionary history. Icarus 201, 44–68. https://doi.org/10.1016/j.icarus.2008.12.019.

Zubarev, A.E., Nadezhdina, I.E., Kozlova, N.A., Brusnikin, E.S., Karachevtseva, I.P., 2016. Special software for planetary image processing and research. ISPRS 529–536, 2016.